The Planetary Science Journal, 4:114 (17pp), 2023 June https://doi.org/10.3847/PSJ/acd10f

Spitzer IRS Observations of Titan as a Precursor to JWST MIRI Observations

Brandon Park Coy[1,2,3,8], Conor A. Nixon[2], Naomi Rowe-Gurney[1,2,4,5], Richard Achterberg[1,2,4], Nicholas A. Lombardo[6], Leigh N. Fletcher[5], and Patrick Irwin[7]
[1] Center for Research and Exploration in Space Science & Technology II (CRESST II), USA; bpcoy0@g.ucla.edu
[2] NASA Goddard Space Flight Center, Greenbelt, MD, USA
[3] Southeastern Universities Research Association (SURA), USA
[4] Department of Astronomy, University of Maryland, College Park, MD, USA
[5] School of Physics and Astronomy, University of Leicester, Leicester, UK
[6] Department of Earth and Planetary Sciences, Yale University, New Haven, CT, USA
[7] Department of Physics, University of Oxford, Oxford, UK
Received 2021 December 14; revised 2023 April 3; accepted 2023 April 26; published 2023 June 27

Abstract

In this work, we present for the first time infrared spectra of Titan from the Spitzer Space Telescope (2004–2009). The data are from both the short wavelength–low resolution (SL; 5.13–14.29 μm, $R \sim 60$–127) and short wavelength–high resolution (SH; 9.89–19.51 μm, $R \sim 600$) channels showing the emissions of CH_4, C_2H_2, C_2H_4, C_2H_6, C_3H_4, C_3H_6, C_3H_8, C_4H_2, HCN, HC_3N, and CO_2. We compare the results obtained for Titan from Spitzer to those of the Cassini Composite Infrared Spectrometer (CIRS) for the same time period, focusing on the 16.35–19.35 μm wavelength range observed by the SH channel but impacted by higher noise levels in the CIRS observations. We use the SH data to provide estimated haze extinction cross sections for the 16.67–17.54 μm range that are missing in previous studies. We conclude by identifying spectral features in the 16.35–19.35 μm wavelength range that could be analyzed further through upcoming James Webb Space Telescope Cycle 1 observations with the Mid-Infrared Instrument (5.0–28.3 μm, $R \sim 1500$–3500). We also highlight gaps in the current spectroscopic knowledge of molecular bands, including candidate trace species such as C_{60} and detected trace species such as C_3H_6, that could be addressed by theoretical and laboratory study.

Unified Astronomy Thesaurus concepts: Titan (2186); Radiative transfer (1335); Natural satellite atmospheres (2214); Saturnian satellites (1427); Transmission spectroscopy (2133); Infrared astronomy (786); Atmospheric composition (2120)

Supporting material: data behind figures

1. Introduction

Saturn's moon Titan exhibits the most complex and diverse atmospheric chemistry of any body in the solar system besides Earth. The bulk atmospheric composition has been estimated at mole fractions of 1.5%–5.5% methane (CH_4) and 98.5%–94.5% nitrogen gas (N_2) depending on altitude (Niemann et al. 2010). Photochemistry in the upper atmosphere produces a rich array of hydrocarbons and nitriles via dissociation of methane and nitrogen gas (Lavvas et al. 2008; Loison et al. 2015). Some oxygen compounds including carbon monoxide (CO), carbon dioxide (CO_2), and water vapor (H_2O) are also produced due to an external oxygen source from Enceladus and contribute heavily to various chemical processes in the atmosphere (Hörst et al. 2008; Dobrijevic et al. 2014; Teanby et al. 2018; Vuitton et al. 2019).

In addition, Titan contains a complex organic haze with a vertical density profile and albedo wavelength dependence that is still not well constrained (Li et al. 2011; Li 2015; Creecy et al. 2019). The haze, primarily composed of organic-rich solid particles, absorbs at visible wavelengths and is transparent at infrared (IR) wavelengths. This leads to an anti-greenhouse effect in which solar radiation is absorbed in the upper atmosphere, whereas thermal IR radiation from the surface escapes easily, reducing the surface temperature by an estimated 9 K (McKay et al. 1991).

Since the 1970s, IR spectroscopy has been a useful tool for probing the composition of the neutral atmosphere of Titan. This has been conducted using ground-based telescopes, visiting spacecraft such as Voyager and Cassini, and space-based observatories including the Infrared Space Observatories. Data from the Voyager 1 Infrared Interferometer Spectrometer and Radiometer (IRIS) provided moderate-resolution observations that led to the identification of previously undiscovered molecules, including diacetylene (C_4H_2), cyanoacetylene (HC_3N), cyanogen [$(CN)_2$], propane (C_3H_8), and propyne (CH_3CCH or C_3H_4; Kunde et al. 1981; Maguire et al. 1981). The Infrared Space Observatory (ISO) Short Wavelength Spectrometer (SWS) offered a resolving power 5–20 times higher than IRIS and led to the discovery of water vapor emission bands near 40 μm and benzene (C_6H_6) at 14.8 μm (Coustenis et al. 1998, 2003). Data from Cassini CIRS were able to map the evolving spatial distribution of molecules as Titan progressed through half its year from 2004 through 2017. However, given that the spectral resolution was comparable to or lower than that of ISO, it did little to provide detection of new molecular species, with propylene (C_3H_6) being the only new molecule discovered on Titan with CIRS so far (Nixon et al. 2013). Propadiene (CH_2CCH_2), an isomer of propyne, has also

[8] Now at the Department of Earth, Planetary, and Space Sciences, UCLA, Los Angeles, CA, USA.

Table 1
Observational Parameters for Select Titan Mid-IR Spectroscopic Observations from Space

Instrument	Exploitable Range (μm)	Approximate Resolving Power	Data Time Span (yr)
Voyager 1 IRIS[a]	7.0–50.0	50–500	1980
ISO SWS Grating Mode[a]	7.0–45.0	1500–3000	1997
Spitzer IRS SL	7.0–11.7	60–127	2004–2006
Spitzer IRS SH	9.9–19.5	600	2004–2008
Cassini CIRS FP1[b]	20.0–1000.0	20–1000	2004–2017
Cassini CIRS FP3[b]	9.1–16.7	1200–2200	2004–2017
Cassini CIRS FP4[b]	7.1–9.1	2200–2500	2004–2017
JWST NIRSpec[c]	0.6–5.3	2700	2022–
JWST MIRI[d]	5.0–28.3	1500–3500	Scheduled (2023–)

Notes. "Exploitable range" refers to the range of the data that showed a high enough S/N for scientific analysis.
[a] Coustenis et al. (2003).
[b] Nixon et al. (2019).
[c] Jakobsen et al. (2022).
[d] Labiano et al. (2021).

Table 2
IRS Module Parameters

Module Name	Wavelength Range (μm)	Resolving Power	Plate Scale (arcsec pixel^{-1})	Slit Dimensions (arcsec)
SL2	5.13–7.60	60–127	1.8	($\sim$3.6–3.7) × 57.0
SL3	7.33–8.66	61–120	1.8	($\sim$3.6–3.7) × 57.0
SL1	7.46–14.29	61–120	1.8	($\sim$3.6–3.7) × 57.0
SH	9.89–19.51	600	2.3	4.7 × 11.3

Note. Despite being reported as constant for the SH module, the resolving power varies slightly with wavelength (Orton et al. 2014a), and this is an approximate value.

recently been detected using data from the ground-based TEXES instrument at the NASA Infrared Telescope Facility (Lombardo et al. 2019b).

The Spitzer Space Telescope (Werner et al. 2004) was the third spacecraft dedicated to IR astronomy after the Infrared Astronomical Satellite and ISO. Spitzer's main telescope contained three instruments: the Infrared Array Camera (Fazio et al. 2004), the Infrared Spectrograph (IRS; Houck et al. 2004), and the Multiband Imaging Photometer for Spitzer (Rieke et al. 2004). Spitzer IRS data have been used to measure the atmospheric compositions of many other solar system bodies, including Uranus (Burgdorf et al. 2006; Orton et al. 2014a, 2014b; Rowe-Gurney et al. 2021) and Neptune (Meadows et al. 2008). Although Spitzer performed multiple dedicated observations of Titan, mostly for calibration purposes, none of the data have been modeled or published before.

The IRS observations largely overlap with those of Cassini CIRS; both are focused on a similar wavelength range and overlap in seasonal coverage. While Cassini CIRS provided a vast amount of information on Titan's atmosphere, Cassini CIRS detector Focal Plane 1 (FP1) exhibited heightened noise levels at the short-wavelength edge of its range ($\sim$17–20 μm; Jennings et al. 2017). The IRS short wavelength–high resolution (SH) observations cover a majority of this noisy region (17.00–19.51 μm) and can provide new moderate spectral resolution coverage in addition to serving as a check on previous CIRS results.

The James Webb Space Telescope (JWST) Mid-Infrared Instrument (MIRI; Rieke et al. 2015) is scheduled to observe Titan and expected to make several improvements over IRS, including a threefold increase in resolving power in the 17–20 μm range ($R \sim 1800$ versus $R \sim 600$) and an over tenfold increase in spatial resolution ($0\farcs20$–$0\farcs27$ pixel^{-1} versus $2\farcs3$ pixel^{-1}), allowing for partial spatial resolution of Titan's disk (diameter $\sim 0\farcs84$). Thus, studying the 17.00–19.51 μm range observed by Spitzer is important for identifying possible spectral features for follow up with MIRI that may have been obstructed by noise in Cassini CIRS observations. Comparisons of the observational parameters of the Spitzer IRS and JWST instruments alongside those of previous IR space-based observations of Titan are shown in Table 1.

In this work, we summarize our data reduction process and spectral retrieval results using Spitzer IRS spectra of Titan. Section 2 describes the observation data format along with the calibration and reduction processes. Section 3 describes the spectral fitting and retrieval process, with Section 4 discussing our retrieval results. Section 5 compares our temperature retrievals with CIRS-based retrievals presented in Teanby et al. (2019) and introduces candidate spectral features for follow-up observations with JWST. Section 6 contains our conclusions and recommendations for future work on Titan.

2. Observations

Spitzer IRS observed Titan in three out of four of its available modules. This includes data from the short wavelength–low resolution (SL; $R = 60$–127, 5.13–14.29 μm), SH ($R \approx 600$, 9.89–19.51 μm), and long wavelength–high resolution (LH; $R \approx 600$, 18.83–37.14 μm) modules. Unlike SL and SH data, flux values in LH exposures were largely inconsistent over separate observations and not used in this analysis (see the Appendix). The diffraction grating of each module splits them into smaller wavelength range "orders." The SH module contains 10 separate orders, and the SL module contains three (SL1, SL2, and SL3). While the SH order data are taken simultaneously, SL data collection is split into two steps (see Section 2.2.1). Table 2 lists various observational parameters for each module.

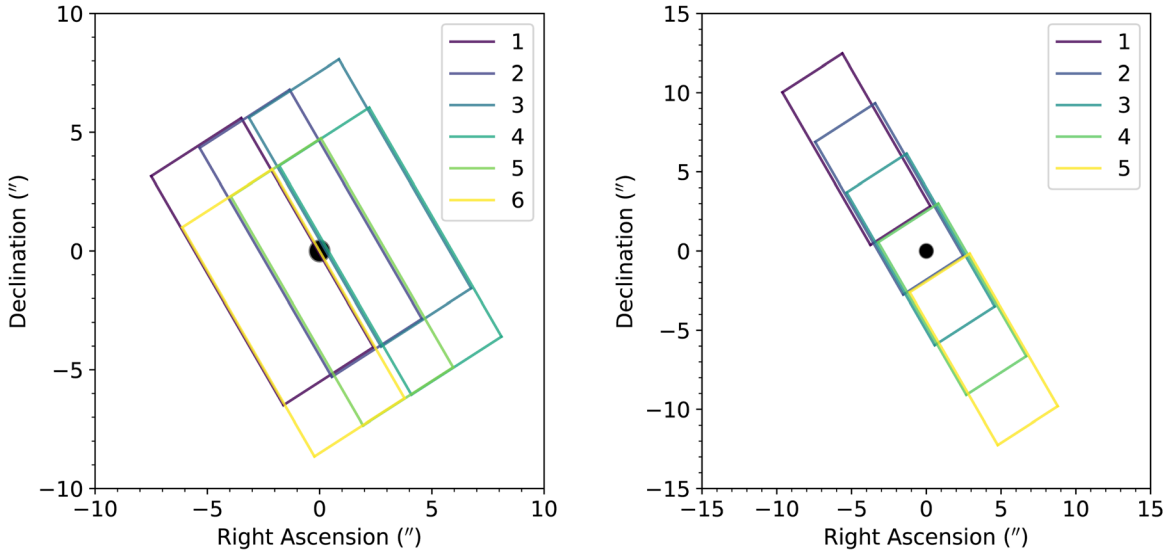

(a) SH module, 2005-11-15, Map Data set 1 (b) SH module, 2005-11-19, Map Data set 2

Figure 1. Example maps of the area captured by the SH module in (a) both parallel and perpendicular mapping steps and (b) only parallel mapping steps in relation to Titan's position observed by Spitzer (black circle). Different colors represent different mapping steps for each session. The R.A. and decl. are reported as the deviation from Titan's center. For map data set 1, steps 2 and 5 had filling factors of 1. Titan was partially captured (filling factor between zero and 1) in steps 1, 3, 4, and 6. For map data set 2, steps 2, 3, and 4 had filling factors of 1. Steps 1 and 5 had a filling factor of zero. For map data set 1, SL observations followed the same mapping layout.

The $\sim 0\farcs84$ angular diameter disk of Titan was much smaller than the $1\farcs8$ and $2\farcs3$ pixel^{-1} scale of the SL and SH modules, respectively, and was thus treated as an unresolved source with the spectra being considered disk-averaged. Data were taken in both the staring and mapping image modes (Section 2.1). A portion of the mapping mode data taken by Spitzer were originally intended to be analyzed for the difference in spectral signatures of the hemisphere containing the "continent" (i.e., Xanadu) seen in near-IR Hubble images and the trailing hemisphere (Houck & van Cleve 2004), but these plans never came to fruition. The remaining Titan data were taken to assist in the calibration of the IRS SH module and were not originally intended for scientific analysis.

2.1. Mapping Mode

The majority of the data used in our analysis were taken in an IRS imaging mode known as mapping mode. As opposed to staring mode, the standard operating mode of the IRS that centers the object in the module's slit, mapping mode took exposures in a grid of map positions around a central object. Data taken over a full grid are referred to as a single cycle. This imaging mode was helpful for extended sources that cover an area of the sky larger than the module's slit dimensions, but when viewed by IRS, Titan is essentially a point source, and thus mapping mode provided few advantages over staring mode. Additionally, when utilizing mapping mode, there is not necessarily a grid position where the target is entirely centered on the slit. This means that Titan was not always centered or even contained within the slit boundaries, leading to a significant drop in brightness in many exposures. Modifications made to the analysis of mapping mode data are discussed in Section 2.1.1.

Unlike stare data, map exposures use a single center position nod and not two separate first and second position nods. This led to a slight modification in the sky subtraction step from the methodology presented in Rowe-Gurney et al. (2021), outlined in Section 2.3.

Given that several observations could be grouped based on certain characteristics, we have split the observations into three distinct data sets: map data set 1, map data set 2, and the stare data set. Observations in map data set 1 contain data from the SL1, SL2, and SH modules and were mapped using a grid of two parallel steps and three perpendicular steps with a step size of $2\farcs4$ over one mapping cycle. Map data set 2 contains data from only the SH module, and the observations were mapped using a grid of five parallel steps with a step size of $3\farcs68$ over four mapping cycles. Example maps for both map data sets can be seen in Figure 1. The stare data set contained standard stare exposures of SH over four cycles. The exposure time was constant for each data set at 6 s exposure^{-1} for both SL and SH, and each module produced 128×128 pixel images.

While it spans a larger time frame than map data set 1, map data set 2 was not used in this analysis, as its average flux standard deviation between exposures within the same observation session (7.8%) was significantly higher than that of map data set 1 (3.1%) and the stare data set (2.0%). The combination of map data set 1 (hereafter the map data set) and the stare data set used in this investigation spans a wide time interval of 2004 March 4 to 2006 April 20. A full list of observation times and various observational parameters is in Table 3.

2.1.1. Filling Factor

Due to problems related to mapping mode, we only used exposures where Titan was completely contained within the slit boundaries. This was done by approximating decl. and R.A. as Cartesian x–y coordinates and calculating the rectangular area encased by the slit boundaries using the specific slit's (see Table 2) dimensions and pointing angle. Titan was then approximated as a circle in the R.A.–decl. plane, with Titan's angular diameter and sky coordinates (relative to Spitzer at the

Table 3
Spitzer IRS Titan Observations

Date	AORKEY	Start Time	End Time	δ_{Titan} (arcsec)	θ_{sep} (arcsec)	No. of Filled Exposures	Model Fit rms Error (%)
Map Data Set (SL, SH)							
2004-03-05	4537856	07:10	07:31	0.8303	191	2 SL and 2 SH	2.9 (SL), 6.8 (SH)
2004-03-25	4538368	15:37	15:57	0.7992	86	2 and 2	5.5 (SL), 6.4 (SH)
2005-11-15	4537600	03:16	03:26	0.7817	52	2 and 2	6.0 (SL), 7.0 (SH)
2006-04-20	4538112	19:48	19:59	0.8178	122	2 and 2	3.8 (SL), 6.8 (SH)
Stare Data Set (SH only)							
2004-03-04	9108992	19:31	19:41	0.8311	185	8	5.3
2004-11-16	12606464	16:06	16:08	0.8200	191	8	5.6
2005-03-23	13360128	22:43	23:01	0.8311	193	8	5.0
2005-04-16	13530112	21:58	22:11	0.7956	192	8	4.9

Note. Times shown are in UTC. The angular diameter of Titan, δ_{Titan}, and angular separation of Titan and Saturn, θ_{sep}, were calculated using the JPL Horizons online interface. Exposures from each observation date were averaged to create one spectrum per observation.

given observation time) retrieved from the Jet Propulsion Laboratory's (JPL) Horizons online solar system data and ephemeris computation service[9] (Giorgini et al. 1996). The full atmosphere of Titan was accounted for by a 425 km (16.5%) increase in its reported diameter, in accordance with the limb extension radius used in Teanby et al. (2013). We assumed that their limb extension radius, derived for Herschel data taken over 32–51 cm^{-1} (196–312 μm), is roughly equal to the limb extension radius for our observed wavelengths. A filling factor, the percentage of Titan enclosed within the approximated slit's boundaries, was then calculated for each exposure. Only exposures with a filling factor of 1 were considered in this work, which accounted for a third of the exposures for map data set 1. Spectra from individual exposures of an observation were then averaged to help remove noise.

Given that Titan is one of the brightest sources viewed by IRS, the SL1 data contained sections of the spectra $\lambda \gtrsim 11.7$ μm that exhibited signs of oversaturation that had not been automatically detected by the IRS Data Pipeline. This was identified by eye through large mismatches with the SH data flux in the overlap ($\lambda = 9.89$–14.29 μm) region. This region was not used for our spectral retrievals. The nonsaturated regions of the SL images did not show signs of significant stray light from the saturated regions.

2.2. Spectral Extraction

Spectral extraction was performed in accordance with Rowe-Gurney et al. (2021) with modifications due to the change in observation target and imaging mode. The software used in the reduction process is available from the Spitzer Science Center[10] (SSC).

Data are available from the Spitzer Heritage Archive (SHA;[11] IRSA 2022) in the form of FITS files of the 2D detector images. We used the first-level basic calibrated data and cleaned them manually, as opposed to using second-level post-basic calibrated data that were automatically cleaned by the pipeline. The SHA data contain masks of historically dead and oversaturated pixels. We used the SSC program `irsclean`'s built-in bad pixel detection method alongside identifying remaining bad pixels by eye. Bad pixels were selected if they were dead or showed large changes in brightness over multiple exposures. In cases with multiple exposures per location (stare data set only), the provided software `coad` was used to coadd the exposures. The SSC program SPitzer IRS Custom Extractor (`SPICE`) was run with default settings to extract spectra from the cleaned and coadded detector images. The SSC program `stinytim v2.0` accounted for overfilling of the slit by Titan's point-spread function (PSF) for 0.5 μm increments of wavelength.

Unlike staring mode observations, SL1 and SL2 data were not taken simultaneously in mapping mode. However, each mapped sky position included separate SL1 and SL2 exposures. These exposures were typically time-separated by 2–3 minutes. When the telescope is utilizing SL1, the other module (SL2) contains blank sky, and vice versa. Therefore, the opposite module (SL1 for SL2/3, and vice versa) was used for sky subtraction. Sky subtraction of SH data was also tested, but the Spitzer campaign lacked dedicated off-source pointings. Due to our relatively high signal-to-background-noise ratio, sky subtraction of other dedicated background campaigns of other targets taken in a close time proximity to the SH observations showed negligible improvement; thus, the process was forgone.

The JPL Horizons interface was used to calculate various parameters pertaining to Titan for each observation, including R.A., decl., angular separation from Saturn, angular diameter, and subobserver latitude. The angular diameter was used to convert the native flux density units of SPICE, janskys, to units of radiance ($W\,cm^{-2}\,sr^{-1}\,\mu m^{-1}$). An effective IR radius of Titan including the atmosphere of 3000 km was used based on assumptions made in Section 2.1.1.

2.2.1. SL Overlap Region

The SL data are split into three orders: SL1 (7.46–14.29 μm), SL2 (5.13–7.60 μm), and SL3 (7.33–8.66 μm). The SL3 data are taken simultaneously with SL2 and treated as a "bonus order," providing a small overlap region (7.46–8.66 μm) with the time-separated SL1 data intended to be used to normalize the SL2/3 and SL1 segments of the spectrum. Given that SL2/3 is more accurate when compared to standard stars according to IRS self-reported error values, the overlap region was used to scale the consistently higher SL1 data to the SL2/3 flux. Scale factors ranged from 0.8% to 10.3% with an average of 3.6%, varying over each observation session. The edges of each order were trimmed, and the three orders were then combined and

[9] https://ssd.jpl.nasa.gov/horizons/
[10] https://irsa.ipac.caltech.edu/data/SPITZER/docs/dataanalysistools/
[11] https://sha.ipac.caltech.edu/applications/Spitzer/SHA/

averaged to create one spectrum. The SH data contained 10 separate orders. The orders are taken concurrently and do not exhibit large amounts of overlap and thus were only trimmed at each order's wavelength range edge and not scaled.

2.2.2. Stray Light from Saturn

Previous observations of Titan have been hindered by stray light reflecting off of Saturn (Coustenis et al. 2002). We accounted for this effect in the low-resolution data through background subtraction of the unused/opposite module. However, the high-resolution exposures lacked such an unused module. Therefore, it was difficult to assess whether stray light from Saturn had a significant impact on the SH data. The angular separation of Titan's center from Saturn's center in each observation ranged from 52″ to 193″, compared to Saturn's ∼21″ angular radius, including its rings. Despite a lack of dedicated background subtraction, there was no statistically significant difference between the flux observed at low and high separation (≪0.1%), suggesting that Titan was far enough for stray light to not display a major impact.

2.3. Errors and Calibration

Errors output by SPICE are not sufficient to account for various systematic sources of error. We used the IRS self-reported error values based on disagreement with standard stars of 4.6% for SL1 and 2.2% for SL2/3 (presented in the IRS Instrument Handbook[12]). Data in the SL1 and SL3 overlap area used the estimated errors of SL1 and SL3 added in quadrature (total 5.1%) to account for additional error introduced by normalization. As the IRS does not self-report a value for SH, the 4% standard deviation reported in Orton et al. (2014a) was used. Average PSF correction factors output by `stinytim v2.0` accounted for an extra 0.88% error in the wavelength range used for the SL module and 0.43% in the SH. These two sources of error were added in quadrature with the SPICE 1σ error to produce an average estimated radiance error of 4.9% in the SL module, 4.0% in the SH module for the stare data set, and 4.1% for the map data set.

3. Spectral Retrievals

3.1. Radiative Transfer Model

Vertical temperature and gas composition profiles were derived using the optimal estimation retrieval algorithm, Nonlinear optimal Estimator for MultispEctral analySIS (NEMESIS; Irwin et al. 2008), which has been used extensively for modeling of planetary atmospheres in the IR, including multiple studies using Cassini CIRS data (e.g., Teanby et al. 2006, 2007; Nixon et al. 2010; Cottini et al. 2012; Lombardo et al. 2019a; Teanby et al. 2019).

Our Titan reference atmosphere contained 99 pressure levels ranging from 1.44 to 10^{-8} bars (0–782 km) and included a pressure–temperature a priori profile for the temperature and gas abundance derived from CIRS data used in Teanby et al. (2009). The gases included in our model are nitrogen (N_2), hydrogen (H_2), carbon dioxide (CO_2), carbon monoxide (CO), water vapor (H_2O), methane (CH_4), hydrogen cyanide (HCN), cyanoacetylene (HC_3N), acetylene (C_2H_2), ethylene (C_2H_4), ethane (C_2H_6), propyne (C_3H_4), propane (C_3H_8), diacetylene (C_4H_2), cyanogen ($[CN]_2$), and benzene (C_6H_6). Propylene (C_3H_6) was also included using a theoretical profile from the photochemical model of Loison et al. (2019). Major isotopologues of methane ($^{13}CH_4$ and CH_3D), ethane ($CH_3^{13}CH_3$), acetylene (C_2HD and $C^{13}CH_2$), carbon dioxide ($^{13}CO_2$, $OC^{18}O$, and $OC^{17}O$), and hydrogen cyanide ($H^{13}CN$ and $HC^{15}N$) were also included. Methane isotopes were separated from each other, whereas all other isotopes were included with their associated molecules.

Retrievals for each separate map data set observation were split into two sequential steps. In the first step, we used the 7.35–9.00 μm (1110–1360 cm^{-1}) region of the SL spectra containing the ν_4 CH_4 spectral band centered at 7.7 μm. Full profile retrievals were run for temperature and haze density, whereas CH_3D was fit for a simple scaling factor. All other gas profiles were kept fixed. The temperature retrieval results were then used as the temperature profile for our second step. As the stare data set did not have accompanying SL data, we skipped this first step and instead used the temperature profile from our original a priori profile.

The second step used the full range of SH data, edge trimmed to 9.96–19.35 μm (517–1004 cm^{-1}), to fit for gas and haze profiles. Full retrievals were done for the haze and C_2H_6 abundances. The C_2H_2, C_2H_4, C_3H_4, C_3H_8, C_4H_2, HCN, HC_3N, and CO_2 profiles were fit by adjusting a single scaling factor. Surface temperature, which is detectable via a low-opacity window at 19 μm (Jennings et al. 2009), was also derived. All other profiles were kept fixed.

3.2. k-Distributions

NEMESIS was run using the correlated *k*-approximation method (Lacis & Oinas 1991) instead of the more computationally intensive line-by-line method. Correlated *k*-tables for each gas were created using both SL and SH wavelength grids reported by IRS with 50 quadrature points to integrate over (*g*-ordinates). Default terrestrial air broadening (similar to N_2) was used in place of the H_2 foreign broadening used in Rowe-Gurney et al. (2021). The *k*-tables were primarily created using high-resolution line lists from the Gestion et Etude des Informations Spectroscopiques Atmosphériques (GEISA; Chedin et al. 1982; Husson et al. 1992; Jacquinet-Husson et al. 2016) 2020 and High-Resolution Transmission Molecular Absorption Database (HITRAN; Gordon et al. 2022) 2020 online line list databases. HITRAN was used for most of the molecules listed in Section 3.1, with GEISA only being used for propyne (C_3H_4) and benzene (C_6H_6), which are not included in the HITRAN database.

A laboratory-derived pseudo–line list created at NASA JPL was used for C_3H_8 (Sung et al. 2013), as GEISA does not include data for all spectral bands included in this study (Nixon et al. 2009). A similar pseudo–line list was also used for C_3H_6 (Sung et al. 2018), which is not included in the current HITRAN or GEISA databases. A Gaussian telescope filter function was calculated for each wavelength assuming a constant $R = 600$ for the SH module and $R = 60$–127, based on wavelength, for the SL module.

3.3. Haze Profile

Initial haze density height profiles were calculated based on findings presented in Tomasko et al. (2008). Using the Huygens probe Descent Imager/Spectral Radiometer instrument data,

[12] https://irsa.ipac.caltech.edu/data/SPITZER/docs/irs/irsinstrumenthandbook/IRS_Instrument_Handbook.pdf

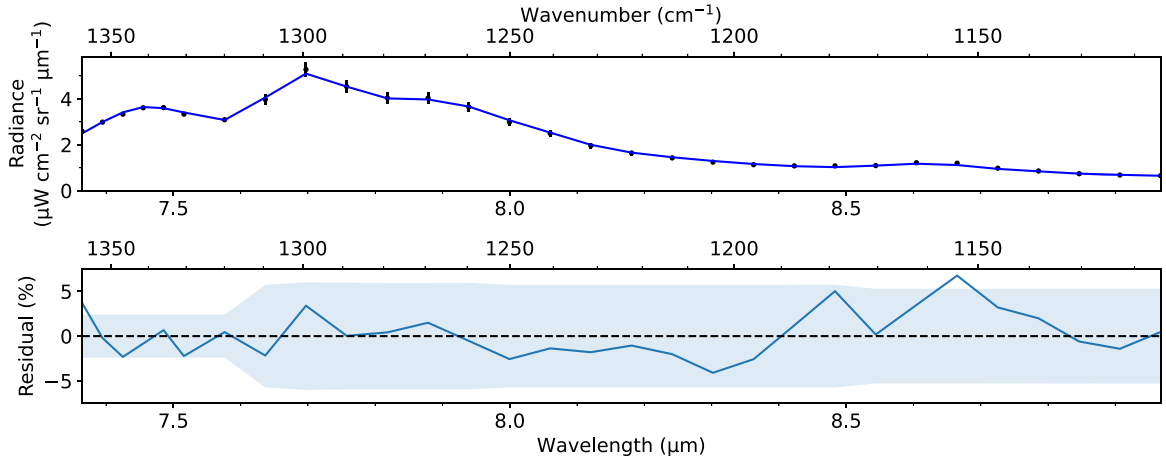

Figure 2. Comparison of the Spitzer IRS SL 2004 March 5 spectrum (black dots) of Titan vs. our NEMESIS model results (blue line). The total spectrum had a reduced χ^2 value $\chi^2/N = 0.32$. Shaded blue regions and black error bars indicate the observational error detailed in Section 2.3. All of the Spitzer SL and NEMESIS model spectra are available as the data behind the figure.

(The data used to create this figure are available.)

they determined that Titan's haze between 60 and 150 km consists of aggregate particles that are composed, on average, of 3000 monomers of radius 0.05 μm. These aggregate particles have a number density of 5 cm^{-3} at a height of 80 km and latitude of 10°S and decrease with a scale height of 65 km. Their data were constrained to a maximum altitude of 150 km. We assumed that this scale height remains constant above 150 km and that their densities measured at 10°S could be approximated in a global average. We used the spectral dependence of the haze particles' refractive indices derived from CIRS data and presented in Anderson & Samuelson (2011) for the 500–560 cm^{-1} (17.9–20 μm) spectral range and Vinatier et al. (2012) for the 610–1500 cm^{-1} (6.7–16.4 μm) spectral range.

3.4. Disk Averaging

The contribution to the disk-averaged spectrum from each observable latitude depends on the observer's field of view. The contribution of Titan's disk and its limb extension were discretized into 20 points, with eight concentric circles across the solid body and 13 across the limb. The field-of-view averaging points used in the creation of our synthetic model spectra were derived from Appendix A in Teanby et al. (2013). Their study assumes a solid radius of 2575 km, with a 425 km limb extension of the atmosphere. We used the same 20 discrete atmospheric paths with weights w defined by the equation

$$w_i = \frac{x_i x_{i+1} - x_{i-1} x_i}{r^2}, \quad (1)$$

where x is the offset from the subobserver point/disk center associated with an emission angle, and r is the effective radius. These weights define the spectral contribution from each of the aforementioned concentric circles and sum to 1.

4. Model Fitting and Interpretation

4.1. Low-resolution Retrievals

An example of our SL retrievals is shown in Figure 2. The methane ν_4-band peak, located at 7.7 μm, was consistently weaker in our retrievals compared to observations. This could be due to sources of localized error not accounted for in Section 2.3. However, χ^2/N values for some retrievals remain significantly lower than 1, indicating that the error self-reported by IRS may be overestimated or only applicable for sources much dimmer than Titan. The rms errors for each fit are shown in Table 3.

Retrieved temperature profiles, an example of which is shown in Figure 3, exhibited a slight heating in the 250–350 km height range up to ~3 K compared to our a priori profile. The implications of this result are discussed in Section 6. Our calculated contribution functions indicate that our temperature retrievals were mostly sensitive to the ~2 mbar (~150 km) region of the atmosphere, in line with previous temperature retrievals presented in Teanby et al. (2006) and Coustenis et al. (2007).

4.2. High-resolution Retrievals

4.2.1. Updated Haze Extinction Cross Sections

Extinction cross-section values for Titan's haze were derived from the refractive coefficients presented in Anderson & Samuelson (2011) and Vinatier et al. (2012). While their data provided coefficients with $\Delta\tilde{\nu} \leqslant 20$ cm^{-1} resolution over the 70–865 cm^{-1} (11.56–142.86 μm) range, the data contain a notable 50 cm^{-1} gap across the 560–610 cm^{-1} (16.39–17.86 μm) range due to higher noise levels in CIRS observations.

Our NEMESIS fits show heightened residuals over the 16.7–17.1 μm range, with a smooth curve indicative of broad haze-like spectral features. NEMESIS deals with gaps in spectral dependencies by linearly interpolating between points. This is a good approximation if the spacing between data points is low but can lead to inaccurate fitting if there is an extended region with no data. Given that this spectral range will soon be observed with JWST MIRI, providing updated extinction cross sections for this region will be useful in separating potential underlying spectral features from the broader haze contribution.

We fit for new cross-section values by comparing the results of our NEMESIS fits using the original Vinatier et al. (2012) cross sections to a gray haze model (equal cross sections at all wavelengths). The gray haze model was run using the average

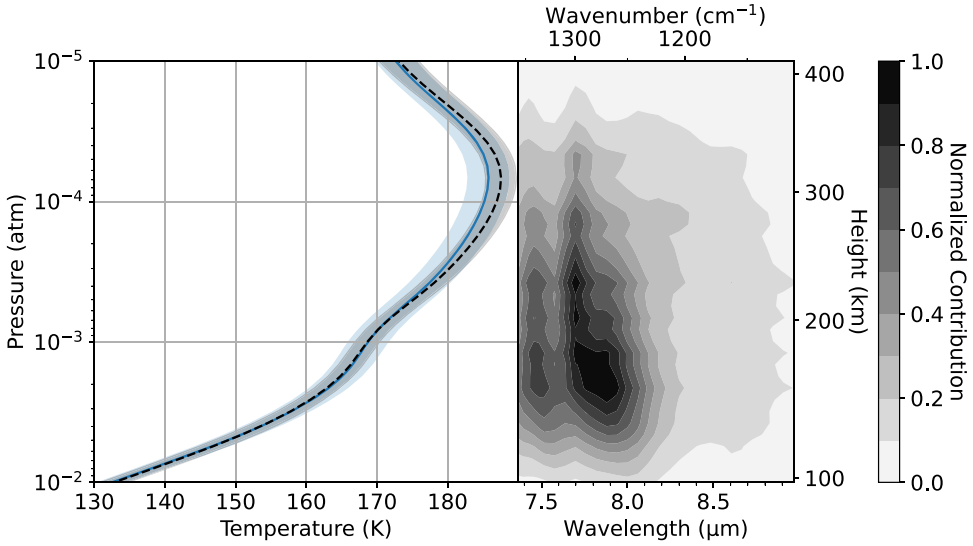

Figure 3. (Left) Accompanying temperature retrieval to Figure 2 output by NEMESIS (black dashed line) compared to our a priori profile (blue line) alongside the normalized contribution function (right). Shaded regions in the retrieved profile indicate the assumed error in our a priori profile (blue) and the fitting error calculated by NEMESIS (black). The contribution peaks at ∼2 mbar (154 km).

extinction cross section of the 560 and 610 cm^{-1} values, $\sigma = 1.6812 \times 10^{-10}$ cm^{-2}. Residuals for each fit were smoothed using a boxcar moving average to remove random noise. A wide width of 16 wavelength steps (∼0.2 μm) was used to ensure removal of possible narrow emission features. We masked the prominent features at 16.39 and 17.35 μm that are possibly due to molecular emission. The difference in residuals between the gray haze and Vinatier et al. (2012)–derived haze was divided by the difference in their cross sections at 520, 530, 540, 550, 560, and 610 cm^{-1} and then averaged for an approximate scaling factor. We then multiplied this scaling factor by our original residuals and added the result to our original cross sections. The results can be seen in Table 4 and Figure 4. Residuals over the 560–610 cm^{-1} range decreased by an average of 60%. These new extinction cross sections were then applied to subsequent SH retrievals.

4.2.2. Wavelength Uncertainties

After analyzing preliminary SH spectral retrieval results, it became apparent that multiple orders exhibited signs of a slight difference in the wavelength reported by the IRS data pipeline and the true wavelength. This suggestion is supported by investigations made in Orton et al. (2014a), which found that wavelengths can vary by up to 20%–25% of a resolution element and that a wavenumber shift of 0.08 cm^{-1} was required to fit the H_2 S(1) quadrupole spectral feature accurately. Analyses based on CIRS data have required a similar wavenumber shift for accurate model fitting (Nixon et al. 2012). This wavelength mismatch is likely due to calibration errors in the SH module arising from minute changes in the telescope's internal temperature or incomplete knowledge of the instrument smoothing function. To counteract this, we fitted both our initial spectral retrievals from NEMESIS and our Spitzer data to cubic splines on a per-order basis. We then found the wavelength "lag" associated with each order through cross-correlation, restricted to within one-fourth of a wavenumber step. We subsequently recalculated our Spitzer cubic spline by shifting our observed wavenumbers by a fitted constant and resampled the new spline for flux values at the original Spitzer wavenumbers. The lags measured ranged from zero (most common) to approximately 16.1% of a wavenumber step. An example wavenumber shift can be seen in Figure 5. This effect is not noticeable in the SL module due to the much lower resolution. The χ^2 values in the areas where this fix was applied were significantly reduced, with an average decrease in the rms fitting error of ∼16% across the observations. However, this fix was difficult to apply consistently, as it was only calculable for regions with order-wide and well-resolved spectral bands, such as the ethane band centered near 12 μm and the acetylene band centered near 13.5 μm.

Table 4
Updated Haze Extinction Cross Sections for the 570–600 cm^{-1} Range

Wavenumber (cm^{-1})	Wavelength (μm)	Extinction Cross Section (10^{-10} cm^{-2})
570	17.544	1.664 ± 0.025(1.631)
580	17.241	1.641 ± 0.016(1.667)
590	16.949	1.546 ± 0.034(1.702)
600	16.667	1.668 ± 0.010(1.736)

Note. Values in parentheses represent the original interpolated values based on Vinatier et al. (2012). Uncertainties were calculated based on the standard deviation across our eight observations.

4.2.3. Retrieval Results

An example NEMESIS retrieval from the high-resolution data can be seen in Figure 6. The rms errors for each fit are shown in Table 3. The error indicated for the SH retrievals is much higher than seen in Section 4.1, particularly in regions with dense spectral bands, discussed below.

4.2.4. Resolving Power Uncertainties

Aside from this wavelength shift, the peaks and troughs of the spectral bands consistently showed residuals above the noise

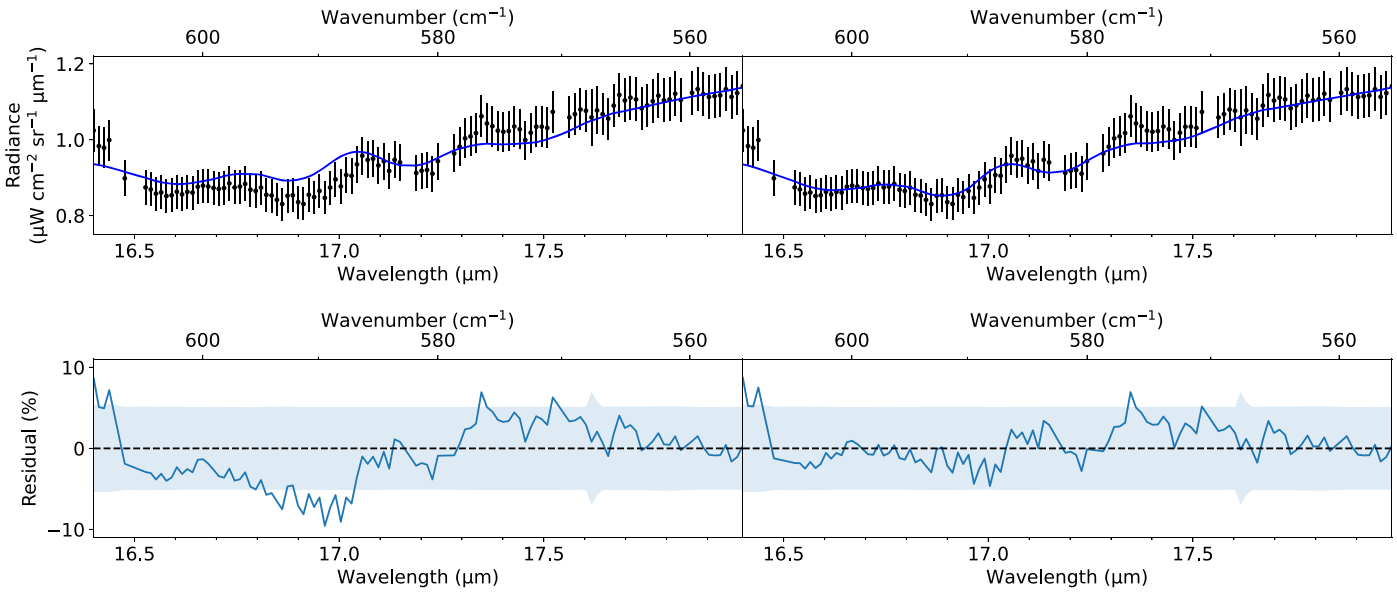

Figure 4. NEMESIS fits for the 2005 November 15 spectrum before (left) and after (right) updating the haze extinction cross sections for the 16.67–17.54 μm wavelength range (Table 4). The updated fit shows significantly better modeling of the broad haze-like features in the 16.5–17.1 μm range while still retaining narrower signatures of possible molecular emission.

level due to an apparent underestimation by our model (see Figure 6). Multiple types of filter function shapes for our *k*-table generation (e.g., Lorentzian, triangular, boxcar) were tested but did not show considerable improvement in peak fitting over the Gaussian filter used in Rowe-Gurney et al. (2021), in line with the results presented in Orton et al. (2014a). Multiple types of gas profile models for ethane and acetylene (e.g., simple scaling factor, pressure gradient, full profile retrieval) were also tested but did not show significant improvement. Similar underfitting of various peaks using NEMESIS can be seen in Rowe-Gurney et al. (2021). Underfitting of peaks is likely due to a difference between the reported resolving power and the actual resolving power of the telescope.

Despite being reported as $R \approx 600$, the resolving power of the IRS is not constant but varies, with a true resolving power $R = 600 \pm 60$ according to the IRS Instrument Handbook.[13] The *k*-tables used in our NEMESIS model assume a constant resolving power of $R = 600$, and variations in resolving power can greatly affect the shape of our model's spectral features. Statically increasing the resolution from $R = 600$ leads to better fitting in underfit regions of the spectra but overfitting of peaks in already well-fit regions of the spectra (see Figure 7), indicating that the resolution varies significantly as a function of wavelength.

Orton et al. (2014b) corrected for this effect by radiometrically scaling down SH data to the lower-resolution SL and LL data and fitting a local resolving power on a per-order basis. They found that for most regions, R only varied as $R = 590$–615, but more dramatic changes in resolving power were observed if they fit the resolving power to specific spectral features, up to $R = 743$. Their fix was possible due to data in the overlap region of the SL and SH modules at 9.89–14.29 μm and the LL and SH modules at 13.98–19.30 μm. However, as the SL data of Titan are oversaturated at wavelengths $\gtrsim$11.7 μm, this fix was not applicable to most of our data. Comparing Spitzer observations of Titan to lower-resolution IR measurements, particularly limb spectra from CIRS, may help in constraining the true IRS resolving power at the ethane and acetylene spectral bands.

[13] https://irsa.ipac.caltech.edu/data/SPITZER/docs/irs/irsinstrumenthandbook/IRS_Instrument_Handbook.pdf

4.2.5. Gas Profile Retrieval Results

Volume mixing ratios (VMRs) for each fitted gas species can be seen in Table 5. We compare our disk-averaged measurements to disk-averaged profiles from the seasonally varying radiative species (SVRS) data set presented in Lombardo & Lora (2023) (accessible on a Zenodo archive at Lombardo & Lora 2022). The SVRS data set includes abundance information for seven molecules (C_2H_6, C_2H_4, C_2H_2, C_3H_4, C_4H_2, HCN, and HC_3N) from the surface to an altitude of over 500 km (1×10^{-8} atm) across all latitudes and over a full Titan year. The SVRS was developed by combining the meridional and seasonal information of the abundance of each molecule at the 1×10^{-3} atm level (about 200 km height) measured with CIRS in Teanby et al. (2019) with the vertical and seasonal information in Mathé et al. (2020); a complete description may be found in Lombardo & Lora (2023). The interpolation scheme used in SVRS enables the calculation of a robust disk-averaged profile for each molecule, which would otherwise be impossible to determine from the discrete CIRS measurements alone. In our comparison, we calculate the disk-averaged SVRS profiles corresponding to 2006 January ($L_S = 313°$) by a weighted sum of abundance profiles across all latitudes. The 1σ uncertainties reported here are the weighted 1σ range of abundances across all latitudes.

Our measurements show a greater abundance in most species than expected from the SRVS-derived disk-averaged profiles. This may be caused by nonlinearities in the radiative transfer scheme that are not accounted for in our simplified disk-averaging calculations, especially due to enrichment of trace species near Titan's winter pole. This enrichment effect has been studied in detail (Hourdin et al. 2004; Teanby et al. 2009, 2017, 2019; Thelen et al. 2019) and is driven by Titan's

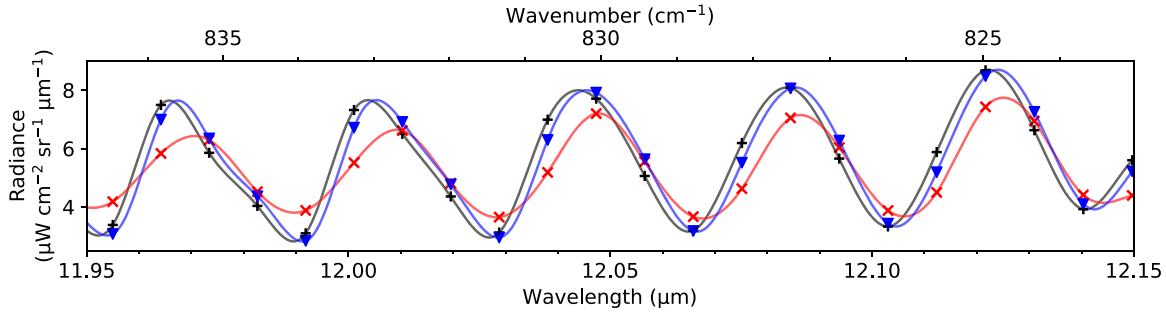

Figure 5. Example results of the cubic spline method described in Section 4.2.2. The observed data (gray) were cross-correlated with our NEMESIS model results (red) to find the wavenumber shift that maximized the cross-correlation factor. The shifted spectrum (blue), redshifted by 0.115 cm^{-1}, shows noticeably better correlation in the spectral band peaks.

stratospheric circulation. A possible inverse relationship between photochemical lifetimes and enrichment factors at the poles has also been proposed (Teanby et al. 2008). This would possibly explain the greater enhancement in our measured HC_3N compared to the SVRS-derived profiles, as HC_3N has a short photochemical lifetime ($\tau < 1$ yr) compared to other hydrocarbon and nitrile species (Teanby et al. 2006).

An additional source of the discrepancy between our measurements and the SVRS-derived HC_3N values may be the method used to determine the disk-averaged profiles from the SVRS data set. Our disk-averaging calculations do not account for the increasing path length through Titan's atmosphere as the distance from the subobserver point increases. Accounting for this effect would lead to an increased weighting of the higher latitudes, including the high winter polar latitudes where HC_3N is enriched. This effect is possibly most noticeable in HC_3N due to the strength of the polar enrichment of this molecule. However, the uncertainties in our HC_3N measurement are on the order of the measurements themselves, indicating that our retrieval is not very sensitive to this molecule.

5. Discussion

5.1. Comparison to Cassini CIRS Data

Temperature profile retrievals for the map data set were compared to the CIRS profiles retrieved in Teanby et al. (2019). They retrieved full temperature profiles for Titan's atmosphere at various latitudes and gas VMRs for C_4H_2, C_3H_4, HC_3N, CO_2, HCN, C_2H_2, C_2H_6, and C_2H_4 at a pressure of 1 mbar (this pressure roughly translated to a 185 km height in our global average) from 2004 July to 2017 September. The specific dates covered were generally within 4 months of our IRS observations. After finding the Teanby et al. (2019) data set closest in time to each of our observations, we used data where the observed Teanby et al. (2019) latitude was closest to the subobserver latitude at the time of observation. Only dates with data points within 10° of the subobserver latitude were used. This was done to approximate a global average, as the Teanby et al. (2019) retrievals were only performed at specific latitudes and generally did not include full hemispheric coverage. Due to only having one data point (at a pressure of 1 mbar) per latitude, the VMR data from Teanby et al. (2019) were too sparse to compare in detail to our gas profile retrievals.

A comparison of our retrieved temperature to that from Teanby et al. (2019) can be seen in Figure 8. The results are generally in agreement, with overlapping 1σ error bars, especially in the high contribution function 100–250 km height range. The warmer temperatures seen at 300–400 km from our retrievals may be due to the warm, elevated stratopause poleward of 50° in the winter hemisphere (e.g., Teanby et al. 2008; Achterberg et al. 2011) contributing to the overall emission in the Spitzer disk-averaged spectra, compared to low-latitude temperature profiles from Teanby et al. (2019), which do not have a warm, elevated stratopause.

5.2. Unmodeled Emission Features and Possible Origins

We noticed two narrow emission features above our assumed noise level that are not well explained by our model spectrum, centered at 17.35 μm (576.2 cm^{-1}) and 16.39 μm (610.2 cm^{-1}), shown in Figure 9. The 17.35 μm feature was also detected in an IRIS-based analysis (Courtin et al. 1995). They postulated that the unidentified emission could be due to a weak H_2O transition near 576 cm^{-1} but noted that this is unlikely due to the overall low concentration of water vapor in Titan's atmosphere and the fact that stronger H_2O bands are not present. Similarly, varying the water vapor profiles in our model did not lead to any improvement in fitting the feature.

5.2.1. Buckminsterfullerene

Neutral buckminsterfullerene (C_{60}) has a well-constrained emission line that is centered at 17.35 μm when in solid phase (Brieva et al. 2016). Production of neutral C_{60} in Titan's atmosphere has been theorized (Sittler et al. 2020) but not detected. In addition, C_{60} has been detected in young planetary nebulae via IRS observations (Cami et al. 2010). However, it is unlikely that a heavy molecule such as solid C_{60} could remain trapped in Titan's atmosphere for a significant amount of time, and we were unable to detect the stronger feature associated with C_{60} at 18.98 μm. Detection of the stronger feature in future studies would greatly help in the identification of C_{60} in the atmosphere.

5.2.2. Polycyclic Aromatic Hydrocarbons

Various species of polycyclic aromatic hydrocarbons (PAHs) have been detected in large abundances in Titan's upper atmosphere (Lopez-Puertas et al. 2013). In addition, certain types of PAHs detected in the interstellar medium exhibit strong spectral features at 16.43 and 17.38 μm with FWHM values of

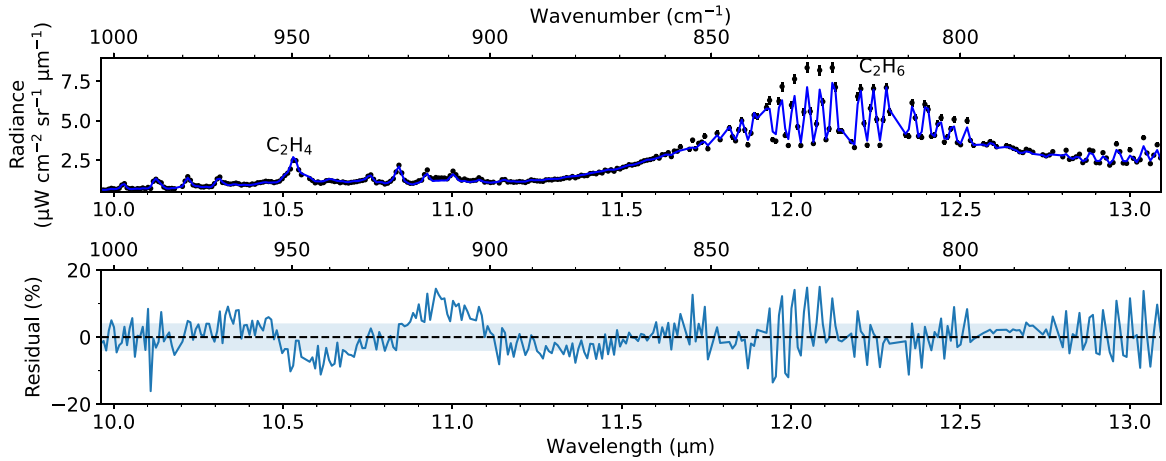

(a) $9.96 - 13.09\,\mu m$

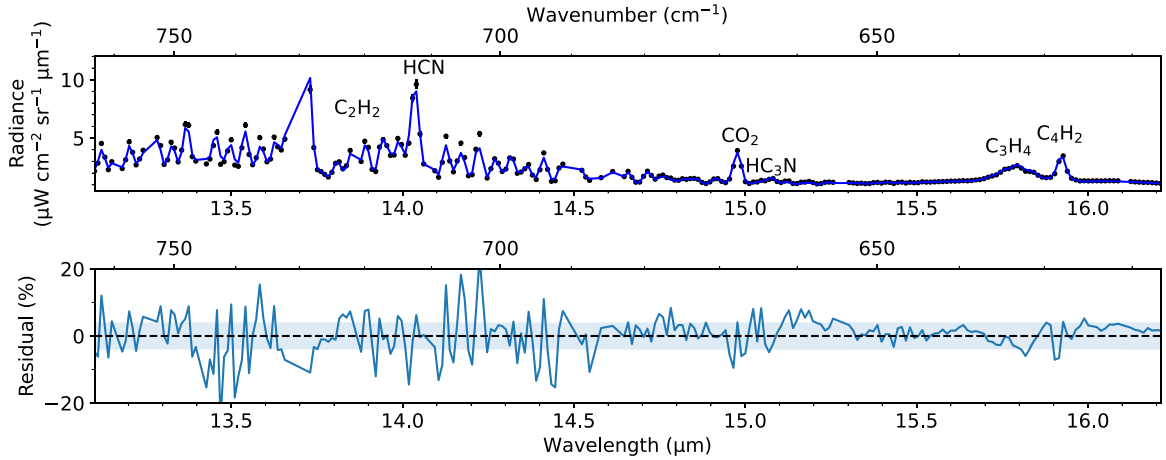

(b) $13.10 - 16.21\,\mu m$

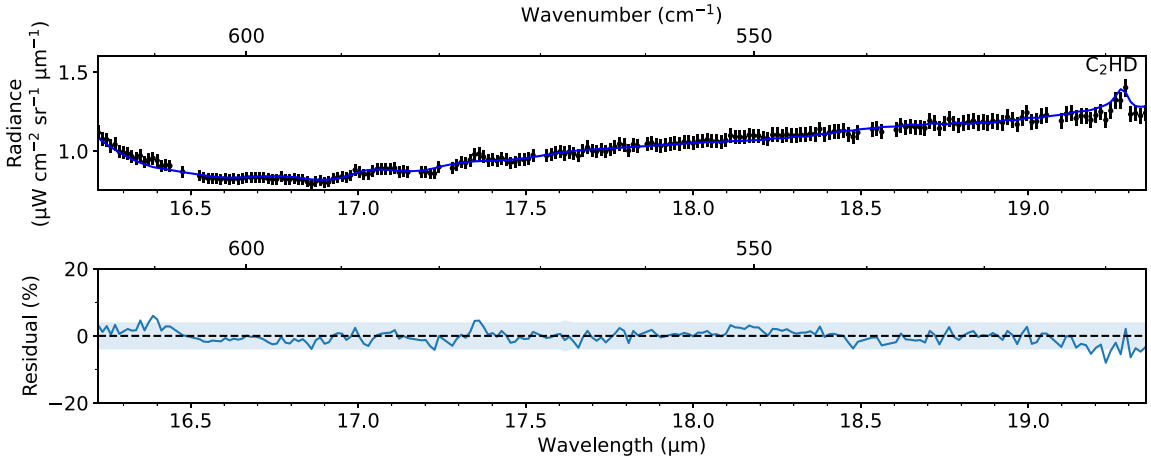

(c) $16.22 - 19.35\,\mu m$

Figure 6. Comparison of high-resolution 2005 April 16 spectra of Titan vs. our NEMESIS model results. The total spectrum had a reduced χ^2 value of $\chi^2/N = 1.50$. Prominent spikes in the residual error can be seen in the ethane and acetylene spectral bands, as well as the band peaks; possible causes are discussed in Section 4.2.2. All of the Spitzer SH and NEMESIS model spectra are available as the data behind the figure.

(The data used to create this figure are available.)

0.16 and 0.13 μm, respectively (Moutou et al. 2000; Peeters et al. 2004). However, these two features are redder than the features observed in our data by about three wavelength steps. The 16.43 μm feature is also predicted to be significantly stronger than the 17.38 μm feature, something not evident in our data.

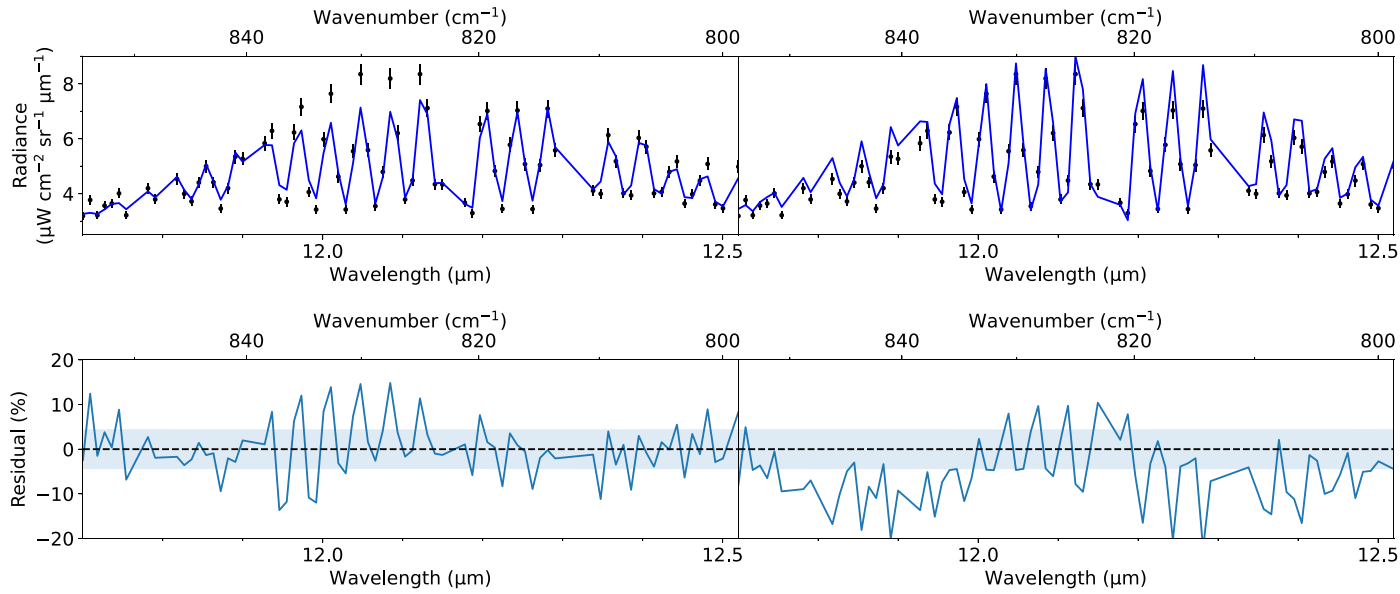

Figure 7. Example model fits (blue) of the C_2H_6 spectral band near 12 μm assuming a constant resolving power of (left) 600 and (right) 720 compared to Spitzer observations (black). Higher resolution leads to significantly lower residuals in originally underfit regions (11.95–12.15 μm) but higher residuals in originally well-fit regions (11.75–11.95, 12.15–12.50 μm). Further studies in the dynamical fitting of Spitzer's true resolving power as a function of wavelength will greatly improve radiative transfer model precision.

The NASA Ames Research Center PAH IR Spectral Database[14] (Boersma et al. 2014; Bauschlicher et al. 2018; Mattioda et al. 2020) contains detailed data on prominent IR transitions of over 4000 types of PAHs. It is unlikely that a single neutral PAH is a perfect match for our observed features. For example, the C_{22} molecule's strongest transition is centered at 17.35 μm but lacks any strong features near 16.39 μm. The C_{33} contains a strong feature centered at 16.38 μm but also a stronger feature centered at 18.18 μm that is not consistent with our data. In addition, the charge of each species shifts where their spectral features are located (Bauschlicher et al. 2008).

Lopez-Puertas et al. (2013) used the PAH database to find that a 3.3 μm emission feature in the upper (900–1000 km) atmosphere could mostly be explained by high concentrations ($\sim 10^4$ cm^{-3}) of the neutral PAHs $C_{48}H_{22}$ and $C_{10}H_8N$. However, these PAHs do not show significant spectral contributions near our unidentified features. A future principal component analysis of the higher signal-to-noise ratio (S/N) and spectral resolution MIRI data using the Ames PAH database, similar to that presented in Lopez-Puertas et al. (2013), may be able to identify the combination of individual molecules that are the source of our spectral features.

Recent studies have attempted to recreate the IR spectral contribution of Titan's organic haze through laboratory experimentation with N_2–CH_4 gaseous mixtures (Dubois et al. 2019; Perrin et al. 2021) but lack coverage in our 16.0–19.5 μm area of interest. A better understanding of the impact of PAHs on Titan's IR spectrum through laboratory experimentation or in situ exploration through the upcoming Dragonfly mission (Lorenz et al. 2018; Barnes et al. 2021) will help constrain the origin of the unmodeled spectral features we see here.

5.2.3. Propylene

The pseudo–line list for C_3H_6 used in our model (Sung et al. 2018) only includes information in the 6.5–15.4 μm (600–1534 cm^{-1}) wavelength range. More recent high-resolution cross-section measurements of C_3H_6 at longer wavelengths have revealed a spectral band centered at 576 cm^{-1} (17.36 μm; Bernath et al. 2023). Since this gas has already been detected on Titan in the IR, this band could potentially explain the missing 17.35 μm emission. However, to check whether it is a good fit, we require a new low-temperature line list or pseudo–line list for this region.

5.3. JWST Cycle 1

JWST is scheduled to observe Titan with MIRI (Rieke et al. 2015) in the 5.0–28.3 μm (350–2000 cm^{-1}) range during its Cycle 1 GTO observations (Nixon et al. 2016, 2021). The primary focus of these observations is the 5–7 μm wavelength range, which has not been observed by CIRS or most other space observatories.

For a given S/N, MIRI is expected to have flux sensitivities $\sim$20–70 times lower than the Spitzer IRS SH module, with an average of $\sim$21 times higher sensitivity in our 16.35–19.35 μm region of interest (see Figure 10). Many of the spectral features observed in the 16.35–19.35 μm range across our IRS observations are very narrow (FWHM of $\sim$two to four wavelength steps) and unresolved. MIRI will have a resolving power of $\sim$2.5–4.5$\times$ that of IRS in the region and $\sim$1.3–2.5$\times$ that of CIRS. Alongside increased resolving power, increased sensitivity will allow for better resolution of the candidate emission features seen in Figure 9 and help confirm these as real features, allowing for further study of their origins. This may also help in the identification of many exotic species active in the IR that are theorized to be produced in the upper atmosphere, as well as aid in further study of previously detected species like C_3H_6 while providing better constraints on the spatial and temporal variations in their abundances. Better spatial resolution will also help in the study of the time dependence of the polar enrichment effect described in Section 4.2.5.

[14] https://www.astrochemistry.org/pahdb/

Table 5

Retrieved Volume Mixing Ratios for Major Gases at Our Observations' Height of Greatest Sensitivity, Determined by NEMESIS Contribution Functions, alongside Retrieved Surface Temperature T_s

Observation Date	T_s (K)	CH_3D	C_2H_2	C_2H_4	C_2H_6	C_3H_4	C_3H_8	C_4H_2	CO_2	HCN	HC_3N
Height (km)		154	124	154	154	154	124	202	124	105	332
Scaling Factor		10^{-6}	10^{-6}	10^{-7}	10^{-5}	10^{-8}	10^{-7}	10^{-9}	10^{-8}	10^{-7}	10^{-8}
Initial values	93.0 ± 1.0	6.60 ± 0.66	2.62 ± 0.52	1.20 ± 0.24	1.27 ± 0.13	0.80 ± 0.16	3.66 ± 0.73	3.03 ± 0.61	1.60 ± 0.32	1.34 ± 0.27	0.21 ± 2.11
2004-03-05	90.1 ± 0.3	7.22 ± 0.72	2.48 ± 0.06	1.82 ± 0.08	1.10 ± 0.07	0.99 ± 0.04	3.66 ± 0.20	4.50 ± 0.34	2.11 ± 0.17	1.17 ± 0.07	1.52 ± 1.20
2004-03-25	90.9 ± 0.3	7.27 ± 0.73	2.55 ± 0.06	1.81 ± 0.08	1.12 ± 0.08	1.00 ± 0.04	3.52 ± 0.19	4.42 ± 0.34	2.04 ± 0.16	1.16 ± 0.07	1.39 ± 1.10
2005-11-15	93.0 ± 0.3	6.63 ± 0.60	2.25 ± 0.05	1.62 ± 0.06	1.02 ± 0.07	0.87 ± 0.03	3.38 ± 0.18	4.31 ± 0.33	1.65 ± 0.11	1.02 ± 0.05	1.68 ± 1.45
2006-04-20	90.7 ± 0.3	6.98 ± 0.67	2.54 ± 0.06	1.66 ± 0.07	1.11 ± 0.07	0.92 ± 0.03	3.49 ± 0.19	4.21 ± 0.30	2.16 ± 0.18	1.10 ± 0.06	1.89 ± 1.64
2004-03-04	91.1 ± 0.3		2.67 ± 0.05	1.73 ± 0.05	1.06 ± 0.07	1.07 ± 0.03	3.24 ± 0.14	4.62 ± 0.30	2.11 ± 0.14	1.20 ± 0.06	1.25 ± 0.78
2004-11-16	90.6 ± 0.3		2.57 ± 0.05	1.67 ± 0.06	1.01 ± 0.07	1.02 ± 0.03	3.18 ± 0.14	4.71 ± 0.31	1.94 ± 0.12	1.12 ± 0.05	1.79 ± 1.25
2005-03-23	90.8 ± 0.3		2.53 ± 0.05	1.63 ± 0.05	1.01 ± 0.06	0.97 ± 0.03	3.11 ± 0.13	4.46 ± 0.28	2.01 ± 0.13	1.06 ± 0.05	1.68 ± 1.13
2005-04-16	90.6 ± 0.3		2.45 ± 0.04	1.65 ± 0.05	1.00 ± 0.07	0.93 ± 0.03	3.11 ± 0.13	4.36 ± 0.27	2.00 ± 0.13	1.04 ± 0.04	1.69 ± 1.12
SVRS, 2006-01			1.74 ± 0.06	1.84 ± 0.34	0.85 ± 0.10	0.90 ± 0.13		3.99 ± 0.64		0.94 ± 0.38	0.19 ± 0.06

Note. Errors represent the fitting uncertainties associated with the NEMESIS retrieval scheme.

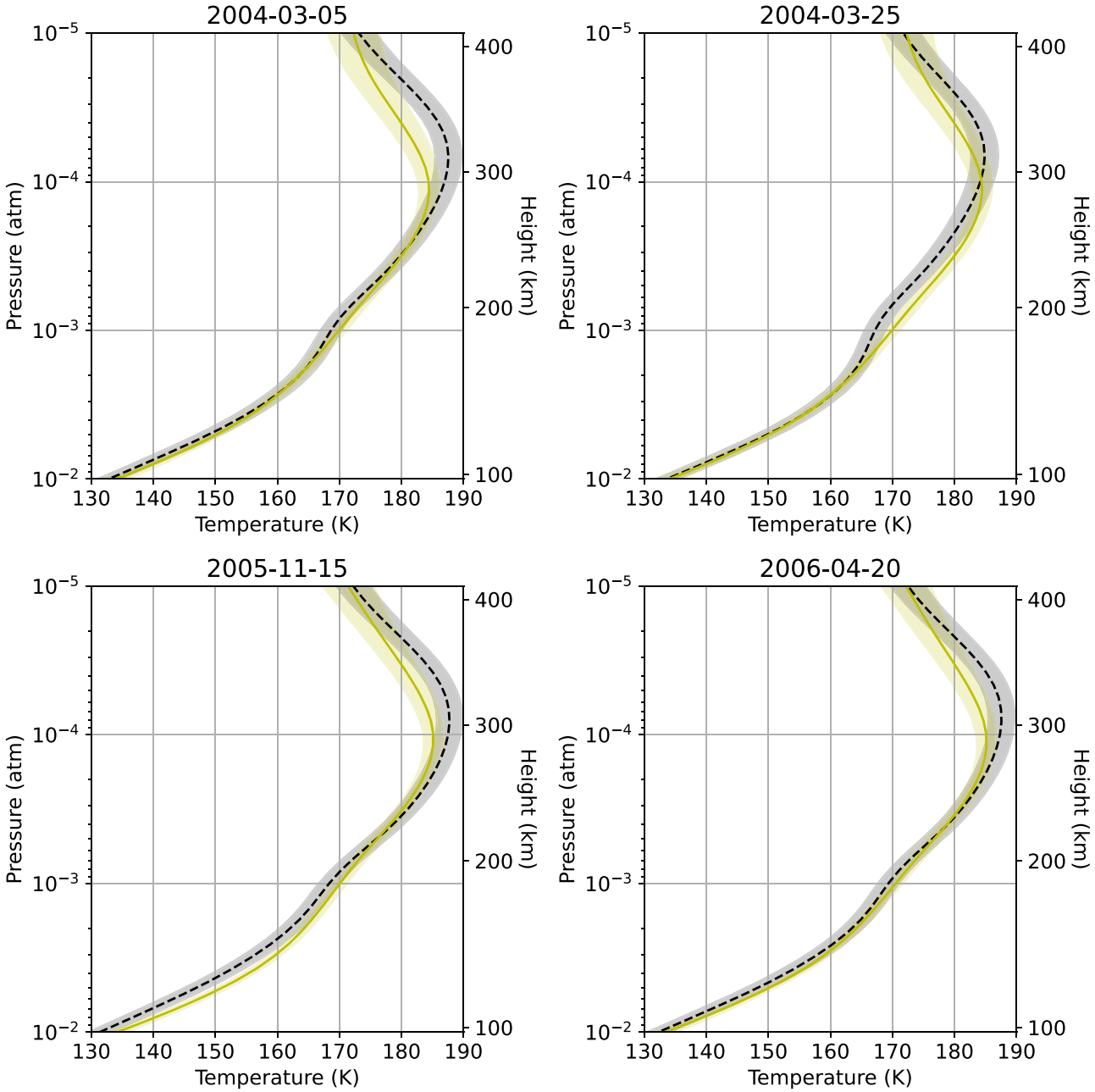

Figure 8. Disk-averaged temperature retrievals for Spitzer data resulting from NEMESIS spectral fitting (black dashed line) compared to similar Cassini CIRS retrievals (yellow line) at the subobserver latitudes listed in Table 6. Shaded regions indicate a 1σ CIRS retrieval error (yellow) and IRS retrieval error (black).

6. Conclusions and Future Work

We performed the first reduction of both high- and low-resolution IR spectra of Titan taken by the Spitzer Space Telescope and made alterations to the spectral inversion algorithm NEMESIS to retrieve various profiles for the disk-averaged spectra of Titan. The data reduction process used in this work largely builds upon Orton et al. (2014a, 2014b and Rowe-Gurney et al. (2021)). The Spitzer data largely confirmed the results derived from previous observations from ISO and CIRS, as well as the haze properties derived in Tomasko et al. (2008), Anderson & Samuelson (2011), and Vinatier et al. (2012). Limitations due to the spatial resolution of Spitzer when compared to that of previous observations made it impossible to measure the spatial variations in our gas and temperature profiles.

Table 6
Summary of the Map Data Set Observation Dates and Subobserver Latitude, L_{obs}, alongside the Closest Date and Latitude in Teanby et al. (2019)

Spitzer Date	Teanby Date	L_{obs} (deg)	Teanby L (deg)
2004-03-05	2004-07-02	−26.24	−25.20
2004-03-25	2004-07-02	−26.28	−25.20
2005-11-15	2005-10-29	−17.07	−15.20
2006-04-20	2006-05-22	−19.98	−20.40

The issues still present in fitting well-known spectral bands, especially in the methane, ethane, and acetylene band peaks, suggest that more work is needed regarding the calibration of IRS observations. Testing of different fitting techniques for the resolving power used in the telescope filter functions required

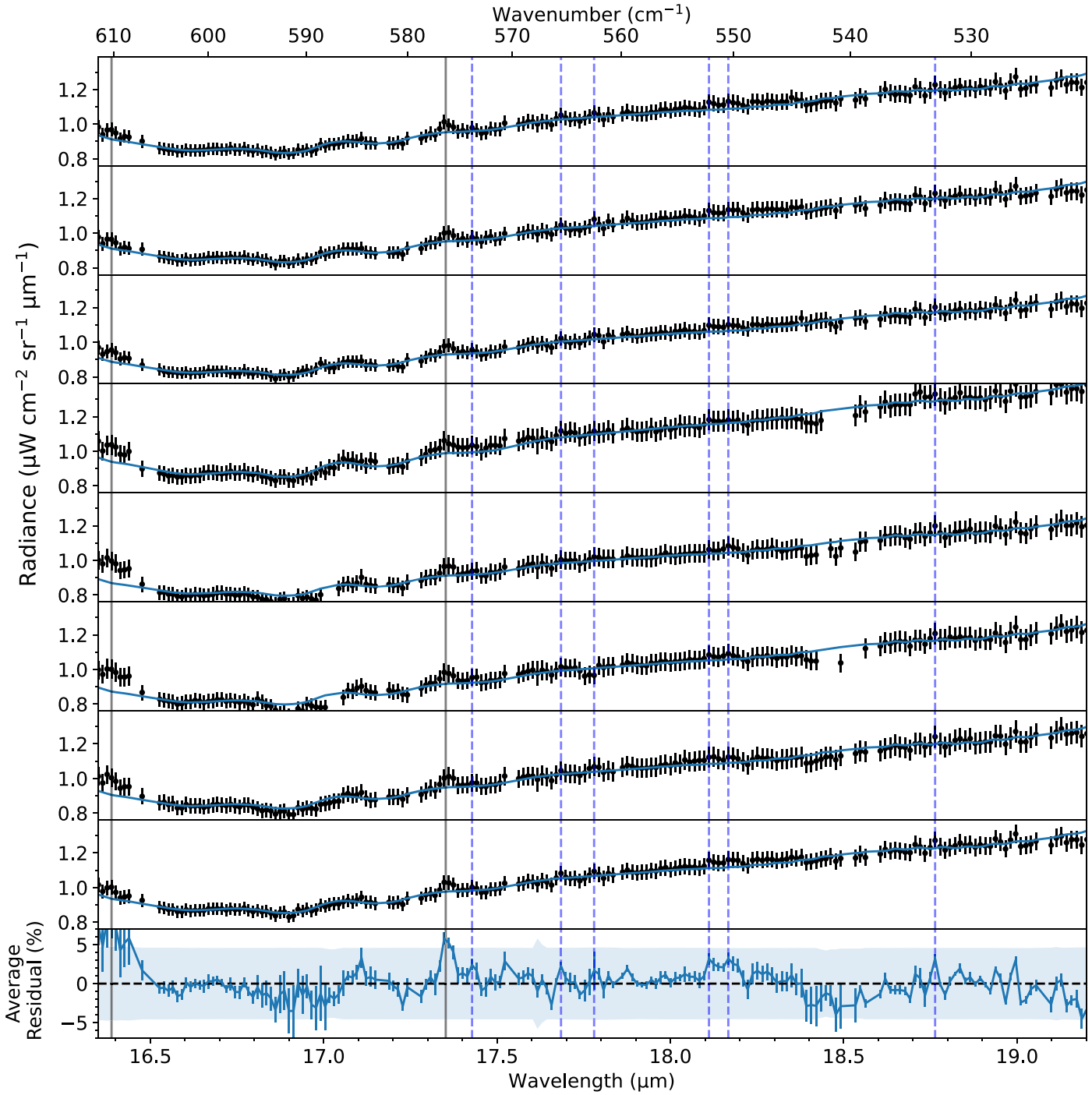

Figure 9. Individual observations (black error bars) and model fits (blue) alongside averaged residuals (bottom) over the 16.2–18.2 μm range. Error bars for the average residuals represent the standard deviation of residuals across the eight observations; smaller error bars represent more consistent features. The shaded blue region represents our estimated noise level. While many narrow spectral features appear to be present across all spectra, the 16.39 and 17.35 μm features (solid lines) are the only candidate features that are consistently above the estimated noise level (∼4%). Dashed lines at 17.43, 17.68, 17.78, 18.11, 18.17, and 18.76 μm represent possible candidate features that may be better resolved through follow-up observations with JWST.

for *k*-table creation could lead to more accurate results. Better constraints on the true error of the IRS data on bright sources would also help us identify more regions of the spectra with fitting issues.

We used the IRS SH data to provide updated estimates for the extinction cross sections of Titan's haze across the 570–600 cm^{-1} (16.67–17.54 μm) range. These updated parameters will be essential in distinguishing the spectral contribution of Titan's haze from underlying signatures of trace gases.

We observed unidentified strong emission features at 16.39 and 17.35 μm and postulated possible chemical species that could explain these discrepancies, including H_2O, C_{60}, C_3H_6, and various PAH species. Several other narrow emission features in the 16.00–19.35 μm range were observed across

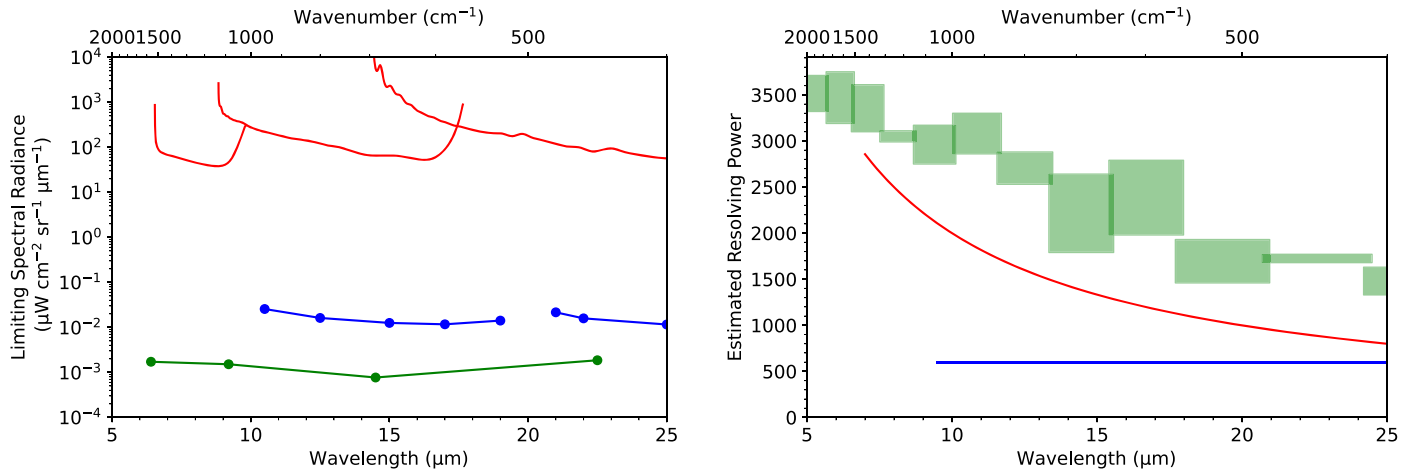

(a) Limiting Signal (b) Resolving Power

Figure 10. (a) Estimated limiting continuum fluxes for the JWST MIRI (green), Spitzer IRS (blue), and Cassini CIRS (red) high-resolution channels for an S/N = 25 signal (equivalent to 4% noise) from a 6 s exposure, based on data compiled by Jane Rigby on the JWST website https://www.stsci.edu/jwst/about-jwst/history/historical-sensitivity-estimates and Flasar et al. (2004). CIRS fluxes were calculated assuming the highest-resolution mode ($\Delta\tilde{\nu} = 0.5$ cm^{-1}). Line fluxes (W m^{-2}) were converted to radiance units by assuming a Titanian angular diameter of $\delta_{\rm Titan} = 0.''81$. The theoretical limiting flux of IRS ($\gtrsim 1 \times 10^{-2}$ μW cm^{-2} sr^{-1} μm^{-1}) is slightly lower than our assumed error ($\gtrsim 3 \times 10^{-2}$ μW cm^{-2} sr^{-1} μm^{-1}) due to accounting for various sources of error other than purely randomized detector noise, including wavelength/resolution shifts and uncertainty in haze parameters. (b) Approximate resolving power R for each instrument over the same wavelength range. MIRI estimates are based on Labiano et al. (2021).

multiple spectra but cannot be confirmed given the moderate resolving power and S/N of IRS. Future investigation of these features through JWST observations used in tandem with pseudo–line lists for the above chemical species will help in narrowing down their origins, as well as improve our understanding of the effects of Titan's haze on our retrieved spectra.

The results we presented here lay the groundwork for JWST MIRI observations of Titan in a spectral window that has been underutilized due to poor data sensitivity in the existing data set. We propose that the following steps be taken to maximize the scientific products from future observations of these spectral windows.

1. The spectral region from 16 to 20 μm lacks low-temperature laboratory spectra of the molecules present in Titan's atmosphere. Cross-sectional measurements should be made to enable the qualitative detection of these molecules in this spectral window from existing Spitzer IRS and future JWST MIRI observations.
2. Pseudo–line lists, similar to those presented in Sung et al. (2013, 2018), for detected and predicted species would enable the proper fitting and retrieval of molecular abundance profiles from these spectral windows. Additionally, these emission bands may be sensitive to different altitude ranges than those observed at higher wavenumbers.
3. The JWST MIRI observations of these spectral windows, with the appropriate updated laboratory cross sections and pseudo–line lists, would potentially enable a more complete vertical description of molecular abundance from ground- and space-based observatories (e.g., Lombardo et al. 2019c).
4. Observations from these spectral windows would help to constrain the hemispheric asymmetry of Titan's stratospheric composition due to the polar enrichment caused by the stratospheric meridional overturning circulation. These constraints would help to elucidate the dynamical changes occurring in Titan's atmosphere as it progresses through its seasonal changes.

Acknowledgments

B.P.C. and C.A.N. were funded by the NASA Astrobiology Institute. B.P.C., N.R.G., and R.A. were further supported by the Center for Research and Exploration in Space Science & Technology II (CRESST II) under NASA award No. 80GSFC21M0002. N.R.G. and L.N.F. were supported by a European Research Council Consolidator Grant (under the EU's Horizon 2020 research and innovation program, grant agreement No. 723890) at the University of Leicester. This work is based on observations made with the Spitzer Space Telescope, which is operated by the Jet Propulsion Laboratory, California Institute of Technology, under a contract with NASA. This research has made use of the NASA/IPAC Infrared Science Archive,[15] which is funded by the National Aeronautics and Space Administration and operated by the California Institute of Technology. Extinction cross-section measurements for C_3H_6 were compiled by Peter Bernath at the Department of Chemistry and Biochemistry at Old Dominion University. The authors give special thanks to Jan Cami of the University of Western Ontario, who was consulted on the spectral features of fullerenes and PAHs and the viability of their existence in Titan's atmosphere.

Data Availability

All data used in this analysis are publicly available online at the SHA[16] by searching "Titan" in the "Moving Object" search option.

Appendix
LH Data

Automated spectra produced by the IRS pipeline (and converted from flux density units to radiance units) for the LH data are shown in Figure 11. The LH data were largely

[15] https://irsa.ipac.caltech.edu/cgi-bin/Gator/nph-dd?catalog=hermesscat500
[16] https://sha.ipac.caltech.edu/applications/Spitzer/SHA/

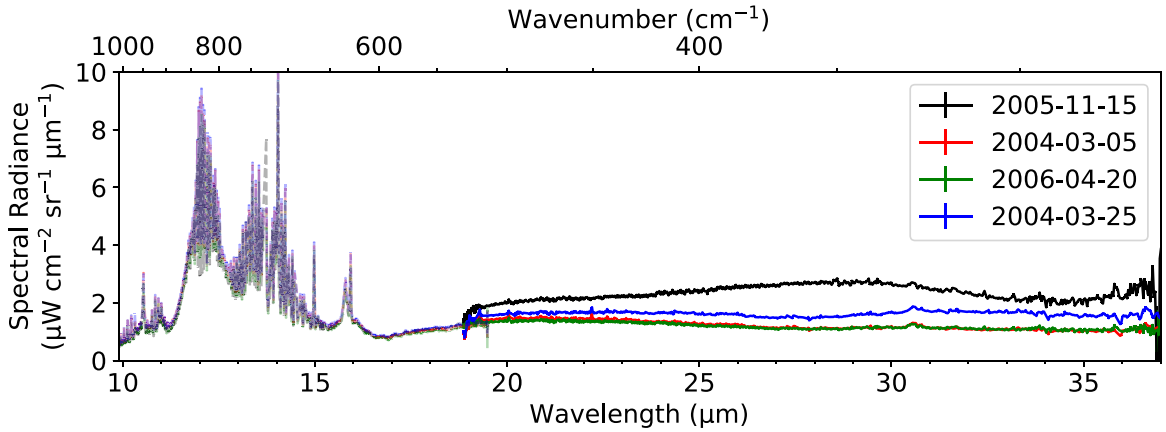

Figure 11. Automated spectra output from the IRS pipeline for the SH (dashed) module alongside their LH (solid) counterparts for map data set 1. Only observations from 2004 March 5 and 2006 April 20 are generally consistent with SL data and each other and may be usable for future analyses of LH data.

inconsistent across observations and discontinuous with SL in overlapping regions; noise reduction techniques were ineffective in changing this result. The reason for these vast discrepancies is not clear. MIRI will allow for better study of the 19.5–28.3 μm region covered solely by the LH module.

ORCID iDs

Brandon Park Coy https://orcid.org/0000-0002-0508-857X
Conor A. Nixon https://orcid.org/0000-0001-9540-9121
Naomi Rowe-Gurney https://orcid.org/0000-0001-8692-5538
Richard Achterberg https://orcid.org/0000-0002-7643-7626
Leigh N. Fletcher https://orcid.org/0000-0001-5834-9588
Patrick Irwin https://orcid.org/0000-0002-6772-384X

References

Achterberg, R. K., Gierasch, P. J., Conrath, B. J., Flasar, F. M., & Nixon, C. A. 2011, Icar, 211, 686
Anderson, C. M., & Samuelson, R. E. 2011, Icar, 212, 762
Barnes, J. W., Turtle, E. P., Trainer, M. G., et al. 2021, PSJ, 2, 130
Bauschlicher, C. W., Jr, Peeters, E., & Allamandola, L. J. 2008, ApJ, 678, 316
Bauschlicher, C. W., Jr., Ricca, A., Boersma, C., & Allamandola, L. J. 2018, ApJS, 234, 32
Bernath, P. F., Dodangodage, R., Zhao, J., & Billinghurst, B. 2023, JQSRT, 296, 108462
Boersma, C., Bauschlicher, C. W., Ricca, A., et al. 2014, ApJS, 211, 8
Brieva, A. C., Gredel, R., Jäger, C., Huisken, F., & Henning, T. 2016, ApJ, 826, 122
Burgdorf, M., Orton, G., van Cleve, J., Meadows, V., & Houck, J. 2006, Icar, 184, 634
Cami, J., Bernard-Salas, J., Peeters, E., & Malek, S. 2010, Sci, 329, 1180
Chedin, A., Husson, N., & Scott, N. 1982, BICDS, 22, 121
Cottini, V., Nixon, C. A., Jennings, D., et al. 2012, Icar, 220, 855
Courtin, R., Gautier, D., & McKay, C. P. 1995, Icar, 114, 144
Coustenis, A., Achterberg, R. K., Conrath, B. J., et al. 2007, Icar, 189, 35
Coustenis, A., Encrenaz, T., Lellouch, E., et al. 2002, AdSpR, 30, 1971
Coustenis, A., Salama, A., Lellouch, E., et al. 1998, A&A, 336, L85
Coustenis, A., Salama, A., Schulz, B., et al. 2003, Icar, 161, 383
Creecy, E. C., Li, L., Jiang, X., et al. 2019, GeoRL, 46, 13649
Dobrijevic, M., HÉBRARD, E., Loison, J.-C., & Hickson, K. 2014, Icar, 228, 324
Dubois, D., Carrasco, N., Petrucciani, M., et al. 2019, Icar, 317, 182
Fazio, G., Hora, J., Allen, L., et al. 2004, ApJS, 154, 10
Flasar, F. M., Kunde, V., Abbas, M., et al. 2004, The Cassini-Huygens Mission (Dordrecht: Springer), 169
Giorgini, J., Yeomans, D., Chamberlin, A., et al. 1996, BAAS, 28, 1158
Gordon, I., Rothman, L., Hargreaves, R., et al. 2022, JQSRT, 277, 107949
Hörst, S. M., Vuitton, V., & Yelle, R. V. 2008, JGRE, 113, E10006
Houck, J. R., Roellig, T. L., van Cleve, J., et al. 2004, ApJS, 154, 18
Houck, J. R., & van Cleve, J. 2004, Observations of Outer Solar System Satellites and Planets, Spitzer Proposal, 71
Hourdin, F., Lebonnois, S., Luz, D., & Rannou, P. 2004, JGRE, 109, E12005
Husson, N., Bonnet, B., Scott, N., & Chedin, A. 1992, JQSRT, 48, 509
IRSA 2022, Spitzer Heritage Archive, IPAC, doi:10.26131/IRSA54
Irwin, P. G. J., Teanby, N. A., de Kok, R., et al. 2008, JQSRT, 109, 1136
Jacquinet-Husson, N., Armante, R., Scott, N., et al. 2016, JMoSp, 327, 31
Jakobsen, P., Ferruit, P., de Oliveira, C. A., et al. 2022, A&A, 661, A80
Jennings, D. E., Flasar, F. M., Kunde, V. G., et al. 2009, ApJL, 691, L103
Jennings, D. E., Flasar, F. M., Kunde, V. G., et al. 2017, ApOpt, 56, 5274
Kunde, V. G., Aikin, A. C., Hanel, R. A., et al. 1981, Natur, 292, 686
Labiano, A., Argyriou, I., Álvarez-Márquez, J., et al. 2021, A&A, 656, A57
Lacis, A. A., & Oinas, V. 1991, JGR, 96, 9027
Lavvas, P. P., Coustenis, A., & Vardavas, I. M. 2008, P&SS, 56, 67
Li, L. 2015, NatSR, 5, 8239
Li, L., Nixon, C. A., Achterberg, R. K., et al. 2011, GeoRL, 38, L23201
Loison, J.-C., Dobrijevic, M., & Hickson, K. 2019, Icar, 329, 55
Loison, J. C., Hébrard, E., Dobrijevic, M., et al. 2015, Icar, 247, 218
Lombardo, N. A., & Lora, J. M. 2022, The Titan Seasonally Varying Radiative Species (SVRS) Dataset, v1.0.0, Zenodo, doi:10.5281/zenodo.7222719
Lombardo, N. A., & Lora, J. M. 2023, Icar, 390, 115291
Lombardo, N. A., Nixon, C. A., Achterberg, R. K., et al. 2019a, Icar, 317, 454
Lombardo, N. A., Nixon, C. A., Greathouse, T. K., et al. 2019b, ApJL, 881, L33
Lombardo, N. A., Nixon, C. A., Sylvestre, M., et al. 2019c, AJ, 157, 160
Lopez-Puertas, M., Dinelli, B., Adriani, A., et al. 2013, ApJ, 770, 132
Lorenz, R. D., Turtle, E. P., Barnes, J. W., et al. 2018, JHATD, 34, 374, https://dragonfly.jhuapl.edu/News-and-Resources/docs/34_03-Lorenz.pdf
Maguire, W., Hanel, R., Jennings, D., Kunde, V., & Samuelson, R. 1981, Natur, 292, 683
Mathé, C., Vinatier, S., Bézard, B., et al. 2020, Icar, 344, 113547
Mattioda, A. L., Hudgins, D. M., Boersma, C., et al. 2020, ApJS, 251, 22
McKay, C., Pollack, J., & Courtin, R. 1991, Sci, 253, 1118
Meadows, V. S., Orton, G., Line, M., et al. 2008, Icar, 197, 585
Moutou, C., Verstraete, L., Léger, A., Sellgren, K., & Schmidt, W. 2000, A&A, 354, L17
Niemann, H. B., Atreya, S. K., Demick, J. E., et al. 2010, JGRE, 115, E12006
Nixon, C. A., Achterberg, R. K., Ádámkovics, M., et al. 2016, PASP, 128, 018007
Nixon, C. A., Achterberg, R. K., Teanby, N. A., et al. 2010, FaDi, 147, 65
Nixon, C. A., Ansty, T. M., Lombardo, N. A., et al. 2019, ApJS, 244, 14
Nixon, C. A., Irwin, P., Sung, K., & Teanby, N. 2021, JWST Proposal. Cycle 1#, 2524
Nixon, C. A., Jennings, D., Flaud, J.-M., et al. 2009, P&SS, 57, 1573
Nixon, C. A., Jennings, D. E., Bézard, B., et al. 2013, ApJL, 776, L14
Nixon, C. A., Temelso, B., Vinatier, S., et al. 2012, ApJ, 749, 159
Orton, G. S., Fletcher, L. N., Moses, J. I., et al. 2014a, Icar, 243, 494
Orton, G. S., Moses, J. I., Fletcher, L. N., et al. 2014b, Icar, 243, 471
Peeters, E., Mattioda, A., Hudgins, D., & Allamandola, L. 2004, ApJL, 617, L65
Perrin, Z., Carrasco, N., Chatain, A., et al. 2021, Processes, 9, 965
Rieke, G., Young, E., Engelbracht, C., et al. 2004, ApJS, 154, 25
Rieke, G. H., Wright, G., Böker, T., et al. 2015, PASP, 127, 584
Rowe-Gurney, N., Fletcher, L. N., Orton, G. S., et al. 2021, Icar, 365, 114506
Sittler, E. C., Cooper, J. F., Sturner, S. J., & Ali, A. 2020, Icar, 344, 113246
Sung, K., Toon, G., Mantz, A., & Smith, M. 2013, Icar, 226, 1499

Sung, K., Toon, G. C., Drouin, B. J., Mantz, A. W., & Smith, M. A. H. 2018, JQSRT, 213, 119
Teanby, N., Bézard, B., Vinatier, S., et al. 2017, NatCo, 8, 1586
Teanby, N., Cordiner, M. A., Nixon, C. A., et al. 2018, AJ, 155, 251
Teanby, N., Irwin, P., de Kok, R., et al. 2006, Icar, 181, 243
Teanby, N., Irwin, P., de Kok, R., et al. 2007, Icar, 186, 364
Teanby, N., Irwin, P., de Kok, R., et al. 2008, Icar, 193, 595
Teanby, N., Irwin, P., de Kok, R., et al. 2009, Icar, 202, 620
Teanby, N., Irwin, P., Nixon, C., et al. 2013, P&SS, 75, 136
Teanby, N., Sylvestre, M., Sharkey, J., et al. 2019, GeoRL, 46, 3079
Thelen, A. E., Nixon, C., Chanover, N., et al. 2019, Icar, 319, 417
Tomasko, M. G., Doose, L., Engel, S., et al. 2008, P&SS, 56, 669
Vinatier, S., Rannou, P., Anderson, C. M., et al. 2012, Icar, 219, 5
Vuitton, V., Yelle, R. V., Klippenstein, S. J., Hörst, S. M., & Lavvas, P. 2019, Icar, 324, 120
Werner, M. W., Roellig, T. L., Low, F. J., et al. 2004, ApJS, 154, 1